EES Batteries

PAPER

View Article Online
View Journal | View Issue

Cite this: *EES Batteries*, 2025, **1**, 185

A highly stable Mn-based cathode with low crystallinity Li_2MnO_3 and spinel functional units for lithium-ion batteries†

Shiqi Liu,‡[a,b,f] Yinzhong Wang,‡[a,b,e] Dongdong Xiao,‡[c] Haifeng Li,[a,b] Tianhao Wu,[a,b] Boya Wang,[a,b] Guangxing Hu,[a,b] Lingqiao Wu,[a,b] Yulong Wang,[a,b] Guoqing Wang,[a,b,e] Nian Zhang[d] and Haijun Yu *[a,b,f]

Received 4th September 2024,
Accepted 6th October 2024

DOI: 10.1039/d4eb00003j

rsc.li/EESBatteries

Mn-based oxide cathodes have emerged as potentially feasible cathode materials for high-specific-energy Li-ion batteries due to their cost-efficiency and exceptionally high capacity *via* the concomitant cationic and anionic redox reactions. However, their practical implementation is still challenging since the trade-off between the electrochemical behaviours and structural stability hinders them from realizing the coinstantaneous high capacity and lifespan. Herein, a structural and crystalline design is introduced into $Li_{0.67}Li_{0.2}[Mn_{0.8}Ni_{0.2}]_{0.8}O_2$, presenting low crystallinity layered Li_2MnO_3 and pre-introduced high-voltage spinel intergrown functional units in the Mn-based composite-structure oxide cathode. This scenario shows no capacity decay within the high-voltage cycling up to 5.0 volt *versus* Li/Li^+, a high energy density of 870 W h kg^{-1}, a low-strain behaviour, and high lithium mobility for high cycling rates. This study provides a solid perspective on the design of Mn-based cathode materials by incorporating distinct functional units and tailoring their configurations, which is conducive to facilitating prolonged Li intercalation chemistry.

Broader context

Mn-based layered oxide cathode materials for lithium-ion batteries (LIBs) have drawn considerable attention in recent years due to their impressive energy density and cost advantages. However, the notorious structural decay during Li^+ ion (de)intercalation would result in decreased electrochemical behaviors upon cycling, which significantly impedes the further development of Mn-based cathodes in batteries. Thus, the establishment of stable composite structures in Mn-based oxide cathodes, except for surface coating and elemental doping scenarios, is an effective and urgent strategy. Highly stable Mn-based cathodes could be realized by the construction of composite structures with pre-introduced spinel structures ahead of the electrochemical processes. In this work, based on a composite-structure Mn-based oxide cathode of $Li_{0.67}Li_{0.2}[Mn_{0.8}Ni_{0.2}]_{0.8}O_2$ with a low crystallinity pre-introduced high-voltage spinel crystal domain incorporated into the parent Li_2MnO_3 layered structure (PHS-LLMNO), the superior electrochemical performance and the structure–activity relationships between the composite structures were revealed thoroughly. The pre-introduced high-voltage spinel crystal domain embedded in the lattice could stabilize the entire material's structures by preventing the gradually emerging metastable phases during cycling, realizing reduced voltage decay, low-strain behaviors, and the crucial maintenance of the electro-active structures. This study illustrates the strategy of pre-introducing a high-voltage spinel crystal domain for efficiently improving the crystal stability during electrochemistry in highly stable composite-structure Mn-based oxide cathode materials.

[a]*Institute of Advanced Battery Materials and Devices, College of Materials Science and Engineering, Beijing University of Technology, Beijing 100124, China. E-mail: hj-yu@bjut.edu.cn*
[b]*Key Laboratory of Advanced Functional Materials, Ministry of Education, Beijing University of Technology, Beijing 100124, China*
[c]*Beijing National Laboratory for Condensed Matter Physics, Institute of Physics, Chinese Academy of Sciences, Beijing 100190, China*
[d]*State Key Laboratory of Functional Materials for Informatics, Shanghai Institute of Microsystem and Information Technology, Chinese Academy of Sciences, Shanghai 200050, People's Republic of China*
[e]*Beijing Create Energy & Benefit Future Co., Ltd, Beijing 100176, China*
[f]*Institute of Matter Science, Beijing University of Technology, Beijing 100124, China*

†Electronic supplementary information (ESI) available. See DOI: https://doi.org/10.1039/d4eb00003j

‡These authors contributed equally to this work.

1. Introduction

Battery-powered devices require cathodes with high specific energy to facilitate the electrification of electrical vehicles and aircraft.[1,2] Moreover, rechargeable Li-ion batteries hold substantial promises for grid energy storage that could accelerate the large-scale use of sustainable energy. These broadly foreseen applications demand the discovery and optimization of intercalation electrode materials to ensure long cycle life and low cost to compete with thermal and hydrogen energy storage for grid applications.[3] Layered oxides with electro-active transition metals (TMs) have the highest capacity among the positive electrode materials, such as $LiCoO_2$, $LiNiO_2$, *etc.*[4–6] However, the resource concerns and the concomitant price issues of cobalt/nickel-based oxide cathodes motivate the exploitation of cheaper ones, resulting in the leap forward of Mn-based oxide cathode materials.[3,7–9]

Among them, Mn-based Li-rich layered oxides (Mn-LLOs) show great capacity exceeding 300 mA h g^{-1} by fully manipulating the abilities of metal cationic redox (MCR) and oxygen anionic redox (OAR) upon cycling, which attract huge attention and receive worldwide resonance.[10–12] It is known that the activities of TM ions and subsequent oxygen redox on charge would influence the mechanisms of the ion migration and structural evolution, resulting in voltage hysteresis and abundant energy loss.[12,13] On the other hand, further irreversible layered-to-spinel/rocksalt transformations, lattice oxygen loss and particle cracking induced by anisotropic mechanical strain will lead to severe structure and capacity decay.[14] Thus, structural design and optimization in Mn-LLOs are potential choices for maneuvering the brilliant electrochemistry.

The structural complexity of Mn-LLOs lies in the bulk and interphase.[15] Due to the reversibility of cation migration, the structural stability of O2-type Mn-LLOs is far better than that of O3-type analogues.[16–19] Moreover, the functional units in Mn-LLOs determine the electrochemical behaviours upon cycling.[20] Thus, the distributions and configurations of these functional units could obviously affect the electrochemistry. Recently, it has been observed that $LiMn_2$ and $LiMn_4$ ordered superstructures in the typical layered oxides, giving rise to the dispersion degree of $LiMn_6$ hexatomic ring configuration in TM layers, exhibit excellent electrochemical performances due to the great lattice-oxygen stability and the ability to prevent the TM disordering processes.[21–26] Despite the importance of bulk structural design, interphase composite constructions are probably scalable and provide intuitive access to realize the performances. Lithium-deficient spinel has high (electro) chemical stability, which could protect the parent layered phase from the destruction caused by corrosive and oxidative species and ameliorate the sluggish kinetics as well as voltage degradation.[27–31] Through pre-introducing spinel structures in the parent layered oxide cathodes with different types, amounts and distributions, multiple electrochemical advantages including enhanced cycling stability, average discharge voltage and inhibition of voltage decay could be achieved.[31] In addition, the formation of metastable phases during cycling could be inhibited effectively with the pre-introduced stable structures. A similar close-packed oxygen framework shared in a layered and spinel structure also dominates the composite structure promise for next uses.

In this work, a highly stable Mn-based composite-structure oxide cathode material fabricated with a pre-introduced high-voltage spinel and Li_2MnO_3 intergrown structure with low crystallinity was investigated. The uniformly and compatibly spread Li_2MnO_3 and pre-introduced high-voltage spinel crystal domains in the lattice of $Li_{0.67}Li_{0.2}[Mn_{0.8}Ni_{0.2}]_{0.8}O_2$ exhibit excellent high-voltage stability, achieving a high energy density of 870 W h kg^{-1} and reliable cycle and rate capabilities with no capacity fading. Importantly, the lattice-matched functional units and the reduced crystallinity contribute to the low-strain property and good Li^+ ion transport kinetics. These results suggest tremendous potential for appropriate use of designing high-quality Mn-based composite-structure oxide cathode materials.

2. Results and discussion

The high-energy $Li_{0.67}Li_{0.2}[Mn_{0.8}Ni_{0.2}]_{0.8}O_2$ composite-structure cathode material with Li_2MnO_3 and pre-introduced high-voltage spinel crystal domains (denoted as PHS-LLMNO) was synthesized by using a facile low-temperature ion-exchange method for the low-temperature synthesized $Na_{0.67}Li_{0.2}[Mn_{0.8}Ni_{0.2}]_{0.8}O_2$ precursor (NLMNO, the XRD refinement result is shown in Fig. S1†). In the entire series of preparation procedures, the synthetic temperatures do not exceed 500 °C (details are provided in the Experimental section), resulting in the composite-structure NLMNO (Fig. 1a, P3-type sodium layered oxide crystal domain and O3-type lithium layered oxide crystal domain) and the composite-structure PHS-LLMNO (Li_2MnO_3 and high-voltage spinel crystal domain).[32–36] Fig. 1b shows the XRD patterns of these two low-temperature synthesized materials, confirming the formation of a composite-structure compound with no observable impurity peaks. The characterized Bragg diffraction peaks are asymmetrically broadened in shape and weakened in intensity due to the low degree of crystallinity achieved under low-temperature conditions. The superstructure peaks at ~21° also show the broadened feature, indicating large amounts of stacking faults exist in the lattice.[35,37,38] Elemental analysis indicates that the as-prepared material is close to the designed compositions (Table S1†). PHS-LLMNO can be Rietveld refined based on a two-phase model in the $C2/m$ space group of Li_2MnO_3 with a = 4.953(5) Å, b = 8.589(9) Å, c = 5.067(2) Å and β = 109.64 (1)° and the $P4_332$ space group of the $LiMn_{1.5}Ni_{0.5}O_4$ (LMNO) high-voltage spinel with a = 8.162(8) Å (details are listed in ESI Table S2†). Fig. S2† shows the TEM images, selected area electron diffraction (SAED) patterns and fast Fourier transformation (FFT) patterns of the representative particles of PHS-LLMNO. The Bragg diffraction spots can be indexed to the $C2/m$ space group of Li_2MnO_3 and the $P4_332$ space group of LMNO, respectively. In addition, the different reflection planes inside the composite-structure units suggest that high

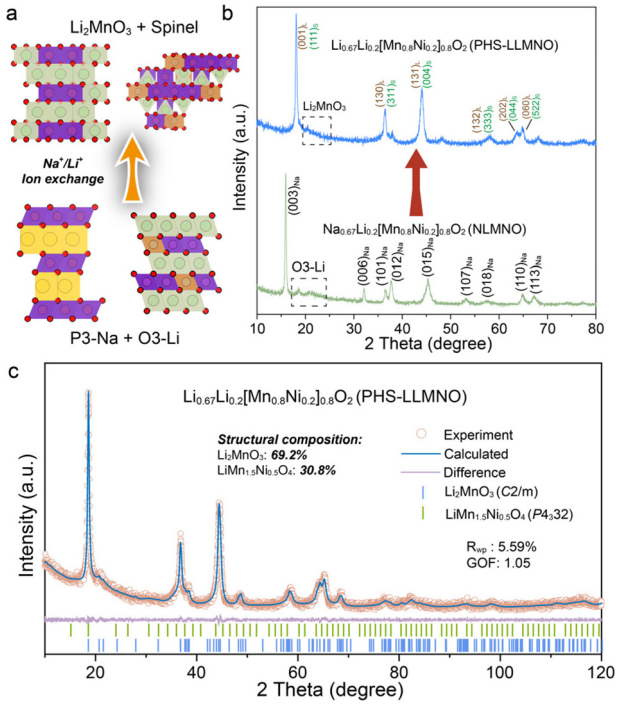

Fig. 1 Crystal structure characterization of PHS-LLMNO. (a) Schematic demonstration of the structural evolution in the low-temperature ion-exchange process. (b) XRD patterns of NLMNO and PHS-LLMNO. (c) XRD pattern of PHS-LLMNO and the corresponding Rietveld refinement results.

density stacking faults of Li_2MnO_3 exist in the bulk (Fig. S2c†), which could efficiently enhance the oxygen redox of the typical Mn-LLOs.[39,40]

The electrochemical behaviours of PHS-LLMNO were examined *versus* Li foil within cut-off voltages of 2.0–5.0 V at different current densities. The PHS-LLMNO cathode can deliver a specific capacity of 257.8 mA h g^{-1} and a high specific discharge energy density of 870 W h kg^{-1} with only 4% irreversible initial capacity loss at 10 mA g^{-1}. On oxidation, the voltage increases with a sloping profile and reaches a plateau at ~4.57 V followed by another sloping region up to 5.0 V. In the subsequent discharge process, the profile shows a typical S-shape discharge curve with two plateaus at 4.7 V and 2.9 V, indicating the electrochemical behaviours of the high-voltage LMNO spinel.[36] In addition, the corresponding dQ/dV and cyclic voltammetry (CV) curves show similar high-voltage spinel features at ~4.7 V (Fig. 2a, inset). According to the dQ/dV profiles of PHS-LLMNO (Fig. S3†) in the following cycles, the reduction peaks upon discharging show a slight shift to a lower potential, indicating the good voltage retention of PHS-LLMNO. Intriguingly, high discharge capacity could be achieved with an average capacity degradation of 0.14% per cycle at 10 mA g^{-1} up to 50 cycles, indicating the excellent high-voltage electrochemical stability of the composite-structure PHS-LLMNO.

Moreover, PHS-LLMNO also exhibits an outstanding rate performance. The gradual increased capacity, shown as an activation process over approximately seventy cycles, is attributed to the slow kinetics of Li_2MnO_3 (Fig. 2b). The PHS-LLMNO cathode can deliver a specific discharge capacity as high as 209 mA h g^{-1} (668 W h kg^{-1}) at 200 mA g^{-1} and 196 mA h g^{-1} (621 W h kg^{-1}) at 300 mA g^{-1} after activation, showing comparable electrochemical behaviours at different rates. After 200 cycles, the capacities show no fading *versus* the initial ones and 87.2/91.3% retention *versus* the activated ones, respectively (Fig. 2b and S4†). The cycling performance of the PHS-LLMNO cathode was also measured with a high mass loading of the active material at a current density of 600 mA g^{-1}, which also shows excellent cycling stability (Fig. S5†). In addition, the degradation of the average discharge voltage for PHS-LLMNO at 300 mA g^{-1} is also slight after long-time cycles (Fig. S6†). In pursuit of evaluating the high-voltage stability of PHS-LLMNO, the recently reported all-fluorinated electrolyte 1 M $LiPF_6$ + 0.02 M LiDFOB in fluoroethylene carbonate, bis(2,2,2-trifluoroethyl) carbonate, and hydrofluoroether (FEC : FDEC : HFE, 2 : 6 : 2 by vol%) was applied in this battery system to stabilize the entire battery system due to the high-voltage and bulk oxygen stability.[41,42] Obviously, the coulombic efficiency of PHS-LLMNO during the cycling is enhanced up to 99.8% and the capacity retention is also improved at a current density of 200 mA g^{-1} after 200 cycles (Fig. S7†), confirming the convincing high-voltage stability and reversible electrochemical behaviours of PHS-LLMNO.

GITT measurement was performed to probe the Li^+ kinetics of PHS-LLMNO. Fig. 2c shows the quasi-open-circuit voltage profile of PHS-LLMNO in the initial two cycles. In particular, this system shows minor polarization with a flat quasi-open-circuit voltage during discharging at the spinel-related working potentials (~4.7 and ~2.9 V) and as tiny as ~46 mV of voltage upsurge, whereas larger overpotentials (>300 mV) are observed in the other medium-voltage region related to the electrochemical processes of the layered structures (Fig. S8†). In general, large voltage polarization during the discharge processes in the normal layered oxide cathodes is obvious, resulting in sluggish Li^+ ion kinetics in a wide voltage range.[23,24] However, PHS-LLMNO maintains similar Li^+ diffusion coefficients of >1 × 10^{-15} cm^2 s^{-1} in the whole voltage range, and noticeably higher Li^+ diffusion coefficients of ~5 × 10^{-15} cm^2 s^{-1} and even a magnitude level of 10^{-14} could be achieved upon discharging at 4.6–5.0 V and ~3.0 V, respectively. Such behaviours originate from the small hysteresis during the oxidation and reduction reactions, and the enhanced Li^+ kinetics is derived from the pre-introduced high-voltage spinel crystal domain in the composite-structure Mn-based cathode.

To elucidate the relationship between the electrochemical behaviours and the distinctive structures, the pristine state of PHS-LLMNO was further deduced by high-resolution high angle annular dark field scanning transmission electron microscopy (HAADF–STEM). The HAADF–STEM image confirms the composite structures in PHS-LLMNO (Fig. 3), which consists of the $C2/m$ Li_2MnO_3 crystal domain and the pre-introduced high-voltage spinel crystal domain in the bulk. Additional images from different particles and areas also

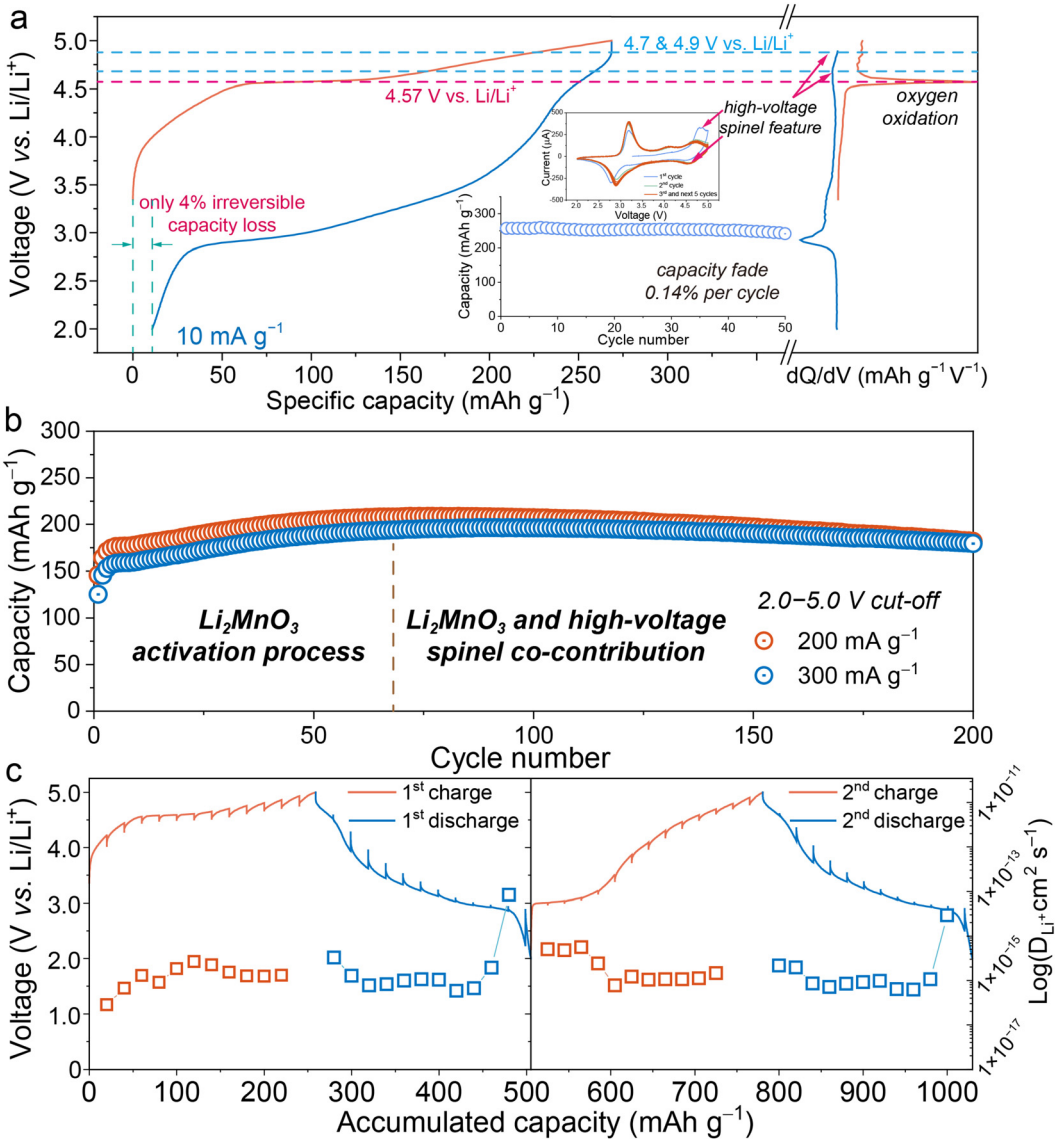

Fig. 2 Electrochemical performances of PHS-LLMNO. (a) The typical initial charge/discharge profile and the corresponding d*Q*/d*V* curves of PHS-LLMNO. The insets show the cycling performance of PHS-LLMNO between 2.0 and 5.0 V at a current density of 10 mA g^{-1} and the CV profiles of the first eight cycles. (b) Capacity retentions at 200 and 300 mA g^{-1} over 200 cycles. The electrolyte used here was 1.1 M $LiPF_6$ in EC : EMC (3 : 7 by vol%). (c) Voltage profiles and Li^+ ion diffusion coefficients of PHS-LLMNO in the galvanostatic intermittent titration technique (GITT) mode within the first two cycles.

further support this universal feature (Fig. S9†), and also show different distributions of these two crystal domains at the surface and in the bulk. In HAADF mode, the atom column intensity is proportional to the atomic number; the bright dots correspond to TM elements and the dark dots are related to Li element features. The atomic-resolution HAADF–STEM images along the [100] zone axis for *C*2/*m* Li_2MnO_3 and the [112] zone axis for $P4_332$ LMNO show two distinct atomic arrangements in the TM and Li layers (Fig. 3a and b). In the layered region, different atomic patterns can be observed, such as the periodic dark-bright-bright-dot patterns (blue frame, region I), and continuous bright-dot patterns (green frame, region II). These features correspond to the ordered Li–Mn–Mn arrangement, that is, the typical $LiMn_6$ hexatomic-ring functional unit and the Li/TM disordered arrangement not only at the surface but also in the bulk.[37] Abundant stacking faults (marked by yellow lines) are found in the Li_2MnO_3 crystal domain, which is consistent with the obvious reflection planes of FFT pattern analysis (Fig. S2c†), and can be attributed to the thermodynamics and the local intrinsic strain in the lattice resulting from low-temperature ion-exchange synthesis.[35] In addition, the large amount of stacking faults in the lattice could also have obvious effects to enhance the TM redox and oxygen activity during the electrochemical cycling, which might contribute to the electrochemical properties of PHS-LLMNO.[38,40] Recent structural and theoretical analyses have uncovered that electro-

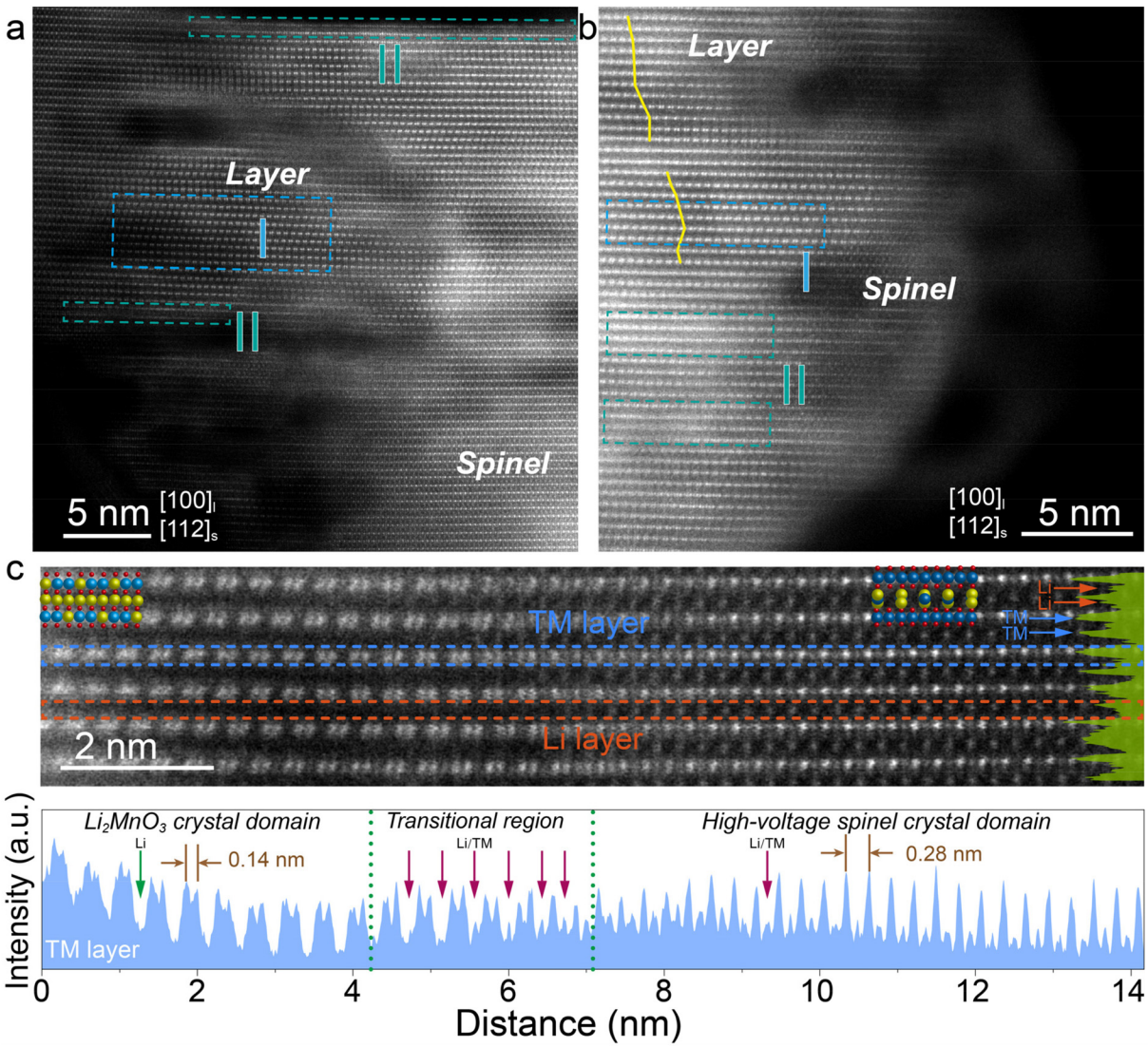

Fig. 3 Atomic structural characterization. (a and b) HAADF–STEM images of PHS-LLMNO. Regions I and II represent the $LiMn_6$ hexatomic-ring functional unit and the Li/TM disordered arrangement, respectively. The stacking faults of 'honeycomb' $[Li_{1/3}Mn_{2/3}]O_2$ layers are traced by the yellow lines. (c) Magnified HAADF–STEM image of PHS-LLMNO based on the *C*2/*m* and $P4_332$ space groups. The peaks in the HAADF–STEM intensity profiles correspond to the selected TM layer. Scale bar, 2 nm.

chemomechanical failures in Mn-LLOs are caused by stacking faults. The high density of these stacking faults in the lattice promotes the formation and spread of microcracks, leading to structural failure.[43] This evidence is highly consistent with our previous understanding on the structural–activity relationships between the density of stacking faults and the oxygen/Mn activity.[30,38] We believed that through rational tailoring of the density of stacking faults, the reversibility of oxygen redox, Mn reduction and the corresponding structural electrochemomechanical degradation in Mn-LLOs could be balanced and the optimized electrochemical performance could be achieved.

Fig. 3c shows the magnified HAADF–STEM image of the intergrowth region of the pre-introduced high-voltage spinel crystal domain (right) and the layered Li_2MnO_3 crystal domain (left) in PHS-LLMNO. In addition, the peaks in the HAADF–STEM intensity profiles reflect the atomic distances of TM layers in each domain. The Mn atoms in the TM layers of the Li_2MnO_3 crystal domain show a typical atomic distance of 0.14 nm, and there are bare TM features in the Li layers, except for the rare Li/Mn antisite defects. In the pre-introduced high-voltage spinel crystal domain, the TM and Li/TM dot features show distances of 0.28 nm and 0.29 nm in the TM and Li layers, respectively, proving the excellent lattice compatible behaviours between each crystal domain. A smooth transitional region connects the above-mentioned domains. The HAADF–STEM peak intensity profile also reflects the gradually changed atomic patterns, showing the generation of the Li/Mn atom column between two TM ions in the TM layer (marked by purple arrows) (Fig. 3c). The pre-introduced high-voltage

LMNO spinel could show functions with diverse electrochemical features for the layered structural unit. However, unlike the well-constructed spinel unit, electrochemically-induced spinel units in the lattice are formed with repeated delithiation and lithiation processes, showing metastable behaviours with unstable possibilities such as TM dissolution and internal stress for the entire structures. Through the rational design of spinel functional units in Mn-based cathodes, the optimized crystal structure and the electrochemical behaviours could be outstanding, which could bring Mn-based cathodes closer to practical applications.

The structural evolution of PHS-LLMNO was revealed by *in situ* XRD and *ex situ* Raman spectroscopy. Here, the *in situ* XRD patterns were obtained using a home-made cell setup between 4.98 and 2.0 V at 20 mA g^{-1} for the initial two cycles (Fig. 4a and S10†). Apparently, there is no emergence of new phases upon electrochemical (de)lithiation. In the initial delithiation process, the $(001)_L/(111)_S$ and $(130)_L/(311)_S$ peaks of PHS-LLMNO slightly shift (<0.5°) to the higher angle, indicating the oxidation processes of the oxygen anion and Ni element, and the concomitant decrease of TM layer spaces, similar to the behaviours of the Li-excess layered cathodes and the cation-disordered rocksalt (DRX)-type materials.[19,44,45] Upon lithiation, the characterized peaks recovered back to the initial positions, indicating the high reversible features in PHS-LLMNO and no over-lithiation phenomenon. In addition, the peak intensity of (001) remains almost constant, demonstrating the stable crystal structures during the electrochemistry.[35] The lattice parameters *a*, *b* and *c* of PHS-LLMNO in Fig. S11† show an exceptionally small change of <1% in the low-voltage range (<4.6 V) and a volume change (ΔV) of ~3% even based on the full voltage range up to 5 V, suggesting the low-strain behaviours, which highly benefits the electrochemomechanically stable composite-structure PHS-LLMNO cathode.[45,46]

The *ex situ* Raman spectra were obtained from the pristine state and the end of the initial charge/discharge states, showing the Li–O stretching mode at ~270 cm^{-1} and the TM–O bonding stretching mode at higher Raman shifts.[47,48] The fitting results show that the two characterized peaks at 593.6 and 645.2 cm^{-1} in the pristine state correspond to the layered and spinel features, respectively. During the charging process, Li^+ deintercalated from the Li layers, resulting in a Li-deficient spinel dominated structure with increased A'_{1g} peak intensity in the corresponding spectra. When the Li^+ ions reversely insert into the lattice, the layered and spinel features are reproduced again with similar behaviours of the pristine state, indicating the highly reversible composite structure in PHS-LLMNO. After 200 cycles, the *ex situ* XRD pattern of PHS-LLMNO shows a decreased intensity of the XRD peak, widened peaks and the peak angle shifting to a higher degree with slight changes in the cycled cathode (Fig. S13†), showing excellent crystal structure stability.

According to the specific electrochemical behaviours, the slope curve in the low-voltage region and the long flat plateau in the initial charge curve correspond to the MCR and OAR processes of PHS-LLMNO, respectively. To study the evolution of the Mn/Ni oxidation states, Mn/Ni L-edge soft X-ray absorption spectroscopy (sXAS) in total electron yield (TEY) mode of PHS-LLMNO was employed (Fig. 5a and c). The surface chemical states could be well elucidated in the TEY mode with a probing depth around 10 nm. During Li^+ ion insertion, the main features of the Mn L-edge do not change apparently, while the higher energy Ni L_3-peak (marked with the pale-yellow frame) increases during charge. Thus, the TM-based capacity contribution of charge compensation is dominated by Ni instead of Mn in the initial charging process. Then the chemical state of Mn was reduced to the $Mn^{2+/3+/4+}$ co-existence state, indicating the partial reduction of the oxidized Mn. To further confirm the evolution of Mn and Ni chemical states in the bulk, hard X-ray absorption spectroscopy (hXAS) of the Mn/Ni K-edge of PHS-LMNO was performed (Fig. 5b and d). Similar evolution trends of Mn/Ni during cycling are shown in the hXAS results, showing the steady Mn K-edge and the right shift of the Ni K-edge during the initial delithiation, indicating the invariant Mn oxidation state and oxidation of Ni to higher oxidation states, and the left shift of the Mn and Ni K-edges upon Li^+ intercalation, reflecting the reduction of both Mn and Ni.

In addition to the chemical state evolution, the local chemical structural variations of Mn/Ni were also demonstrated by the Fourier transformation of the Mn/Ni K-edge extended X-ray absorption fine structure (EXAFS) analysis (Fig. 5e and f). Compared to the pristine state, the intensity of the signal of Mn–O interactions greatly decreased and the average Mn–O distance greatly increased in the charged states, which might indicate the increased disorder degree of the first Mn–O shell and the reconstruction of O–O interactions and the emergence of Mn vacancies.[44] While the Ni–O/Ni–TM interactions of PHS-LLMNO maintain good reversibility both in magnitude and in distance upon charging/discharging, which leads to good structural stability in high-voltage working environments and boosts the excellent electrochemical behaviours. In par-

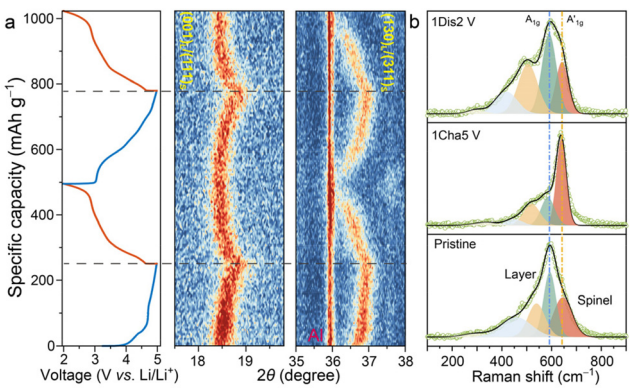

Fig. 4 Structural and phase evolution of PHS-LLMNO during cycling. (a) Selected *in situ* XRD 2D contour patterns and voltage profiles of PHS-LLMNO during the initial 2 cycles. (b) *Ex situ* Raman spectra of PHS-LLMNO at pristine, fully charged and fully discharged states in the initial cycle.

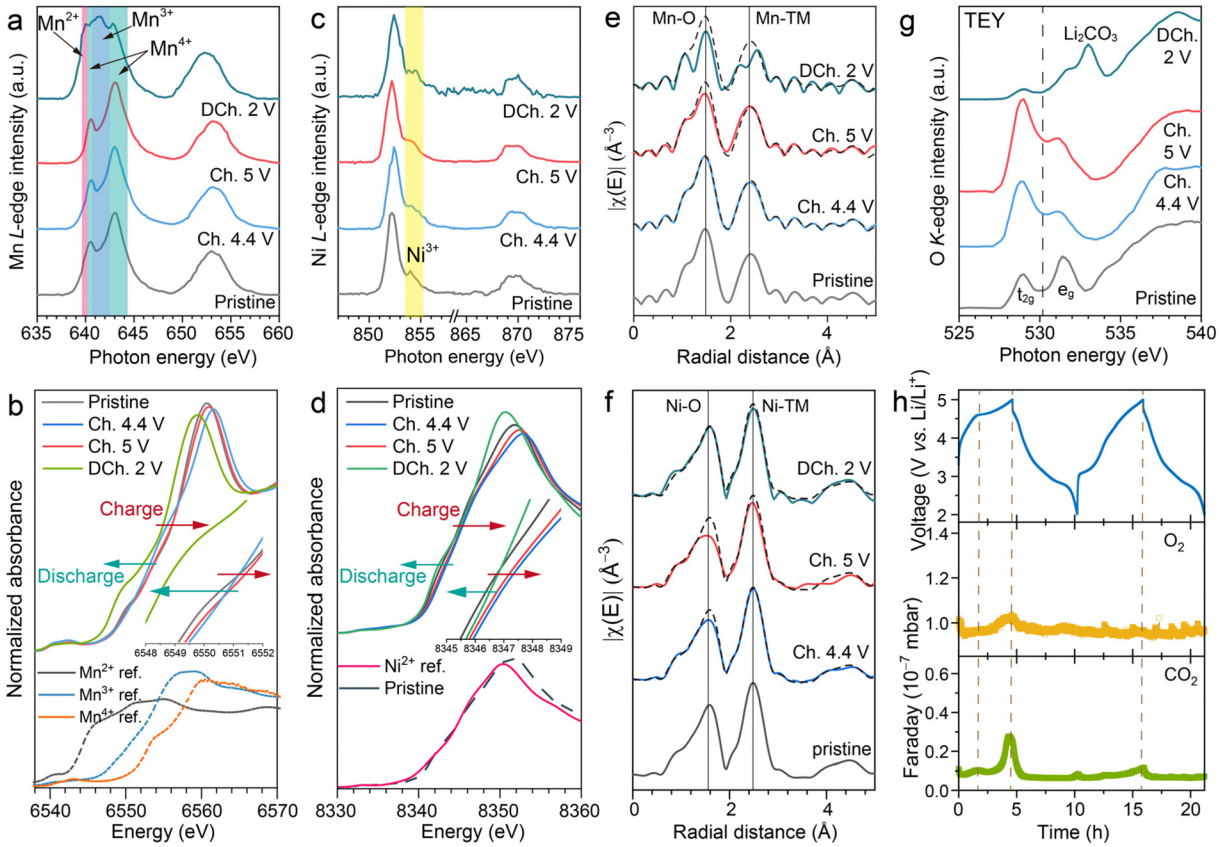

Fig. 5 Charge compensation mechanisms of PHS-LLMNO. *Ex situ* sXAS spectra of Mn (a) and Ni (c) L-edges at different electrochemical states. *Ex situ* hXAS spectra of Mn (b) and Ni (d) K-edges at different electrochemical states. Evolution of K_2-weighted Fourier transform magnitudes of the (e) Mn and (f) Ni K-edge EXAFS spectra; the EXAFS spectra obtained in the pristine state are also offset and overlaid in a black dashed line for comparison. (g) *Ex situ* sXAS spectra of O at different electrochemical states. (h) *In situ* DEMS of the gas evolution rate during the initial two cycles.

ticular, the wavelet transforms (WTs) of the Mn/Ni K-edge EXAFS spectra (Fig. S13†) were generated to further reinforce the coordination of structural evolution.[49] WT analyses of all measured *ex situ* states in PHS-LLMNO show that the first coordination shells of TM–O/TM–TM are maintained at the same location compared with the pristine state, and the WT magnitude is reversible, which suggests the highly stabilized local covalent structures derived by the pre-induced high-voltage spinel strategy, further boosting the excellent electrochemistry of PHS-LLMNO.

sXAS in TEY mode and *in situ* differential electrochemical mass spectrometry (DEMS) analyses were used to study the chemical evolution and to investigate the irreversible O_2 and CO_2 gas generation in charging/discharging states in PHS-LLMNO. As for the OAR of PHS-LLMNO, the pre-edge peak intensity increases obviously from the pristine state to 5.0 V (Fig. 5g). According to the stable Mn oxidation state upon charging (Fig. 5a), the increased pre-edge intensity could be ascribed to the oxygen oxidized features.[50] Besides, the 533 eV peak at the end of discharge (2.0 V) is derived from the electron transitions between the O 1s and unoccupied $\pi^*_{C=O}$ orbitals in carbonates of the newly emerged Li_2CO_3.[50] The interfacial evolution during the high-voltage operation was detected by *ex situ* XPS (Fig. S14†). The content of carbonate species would increase at the interface on discharging, which indicates the generated by-product after the high-voltage operation due to the decomposition of the electrolyte. Meanwhile, the release of O_2 and CO_2 was detected by the *in situ* DEMS technique during the initial two (de)lithiation processes (Fig. 5h). It was found that a small amount of O_2 gas was released in the high-voltage region, which is contributed by the irreversible oxidation of the oxygen components from the lattice oxygen. In addition, the CO_2 gas generation is derived from the degradation of the electrolyte at ultrahigh working potentials.[51,52] The notorious O_2 and CO_2 gas release process was effectively restrained in PHS-LLMNO in the 2nd charging process, which is consistent with the highly reversible electrochemical processes (the fluctuation of the oxygen signal is derived from pressure changes of the testing room). It should be noted that the onset of O_2 generation begins at ~4.68 V, which is higher than that of previous works on common Mn-LLOs, indicating the high-voltage and oxygen redox reaction stability of the Mn-based composite-structure PHS-LLMNO cathode.[52–55]

3. Conclusions

In conclusion, the electrochemistry of an Mn-based composite-structure oxide cathode could be significantly improved by intergrown functional unit fabrication with a pre-introduced high-voltage spinel and layered Li_2MnO_3, which was constructed by a facile low-temperature synthesis method combining the molten-salt ion-exchange method. Following this design strategy, highly stable electrochemical behaviours upon cycling were obtained for the highly stable PHS-LLMNO, with reversible structural change and low lattice strain, key factors for stable electrochemical operation that has been proved in the typical layered oxides. Furthermore, the charge compensation mechanisms proved the distinct functions for each unit in the lattice, showing the stabilization effects of the pre-introduced high-voltage spinel in the lattice. These discoveries provide great benefits and opportunities for the realization of both high specific energy and long cycle life in Mn-based oxide cathode materials with the composite-structure construction.

4. Experimental section

4.1 Materials synthesis

The $Mn_{0.8}Ni_{0.2}(OH)_2$ precursor was prepared by a co-precipitation method using transition metal sulfate aqueous solution (Mn/Ni molar ratio: 8/2); the details are shown in the previous reports.[51,56] The hydroxide precursor was first mixed with stoichiometric amounts of Na_2CO_3 and Li_2CO_3. Then the low-temperature NLMNO was synthesized by calcining the mixture at 500 °C in air for 48 h.

PHS-LLMNO was synthesized through a facile low-temperature ion-exchange method from the as-prepared NLMNO sample in $LiNO_3$ and LiCl (molar ratio 88/12) molten salts. After mixing in a mortar for >30 min, the mixture was calcined at 280 °C in air for 6 h. Then the as-prepared PHS-LLMNO was washed 3 times with distilled water and dried at 100 °C under vacuum overnight.

4.2 Characterization

XRD patterns of the as-prepared samples were obtained using a D8 Advance powder X-ray diffractometer (Bruker) with Cu Kα radiation (λ = 1.5406 Å). Rietveld refinement was performed using TOPAS5 software. For the *in situ* XRD measurement, a home-made *in situ* cell with an X-ray transparent beryllium window was used, and each pattern (from 15° to 50°) was collected every 20 min while the cell was operated at a current of 20 mA g^{-1}. High-resolution TEM imaging and selected area electron diffraction were performed using a JEOL-2100F electron microscope operating at 200 kV. Atomic resolution high-angle annular dark field scanning transmission electron microscopy (HAADF–STEM) images were obtained using a probe aberration-corrected JEOLARM200CF electron microscope equipped with a cold field emission gun operating at 200 kV. The convergent angle and collection angle for HAADF–STEM imaging were 28 mrad and 90–370 mrad, respectively. Raman spectra of the pristine and cycled electrodes were recorded with a Raman spectrometer (WITec-alpha300R) using a 532 nm laser source in an Ar-filled glove box. *In situ* differential electrochemical mass spectrometry (DEMS) measurements were performed using a customized DEMS device to monitor the evolution of O_2 and CO_2 gases upon cycling with a current density of 50 mA g^{-1}. O K-edge and Mn/Ni L-edge XAS measurements were performed at beamline BL02B02 of the SiP·ME^2 platform at the Shanghai Synchrotron Radiation Facility (SSRF). The *ex situ* hXAS measurements of Mn/Ni K-edge spectra were performed at beamlines BL11B and BL14W1 of SSRF.

4.3 Electrochemistry

The electrodes were prepared by mixing the active materials with carbon black and the polytetrafluoroethylene (PVDF) binder in a weight ratio of 80 : 10 : 10. The mass loading of the active material was 3 mg cm^{-2}. The coin cell was assembled using the cathode film, the electrolyte, separators (Celgard) and lithium metal foil in an Ar-filled glove box. The electrolyte used was 1.1 M $LiPF_6$ in ethylene carbonate : ethyl methyl carbonate (EC : EMC, 3 : 7 by vol%) and 1 M $LiPF_6$ + 0.02 M LiDFOB in fluoroethylene carbonate, bis(2,2,2-trifluoroethyl) carbonate, and hydrofluoroether (FEC : FDEC : HFE, 2 : 6 : 2 by vol%). The galvanostatic cycling tests were performed at 25 °C using NEWARE and LAND testers. The GITT was performed at 20 mA g^{-1} between 2.0 and 5.0 V using a Neware battery test system (CT-4008, Shenzhen, China). The *ex situ* (de)lithiated samples were prepared by charging/discharging the cells at 20 mA g^{-1}, and then the cathode films were washed with dimethyl carbonate (DMC) and collected in an Ar-filled glove box. The cyclic voltammetry test was performed on a Solartron electrochemical workstation.

Author contributions

Conceptualization: H.J.Y., S.Q.L., Y.Z.W., D.D.X., and Y.L.W.; investigation: S.Q.L., Y.Z.W., D.D.X., G.X.H., G.Q.W. and N.Z.; formal analysis: S.Q.L., Y.Z.W., D.D.X., T.H.W., B.Y.W., L.Q.W. and Y.L.W.; writing – original draft: S.Q.L.; writing – review and editing: S.Q.L., Y.Z.W., D.D.X., H.F.L. and H.J.Y.; supervision: H.J.Y.

Data availability

The data supporting this article have been included as part of the ESI.†

Conflicts of interest

The authors declare no conflict of interest.

Acknowledgements

This work was financially supported by the National Key R&D Program of China (No. 2022YFB2404400), the National Natural Science Foundation of China (No. 92263206, U23A20577, 52372168 and 21975006), The Youth Beijing Scholars Program (No. PXM2021_014204_000023), and the Beijing Natural Science Foundation (No. 2222001 and KM202110005009). The authors appreciate the help and guidance of the beamline staff on beamlines BL02B02, BL11B, BL14B1 and BL14W1 at SSRF, Shanghai, China.

References

1 V. Viswanathan, A. H. Epstein, Y. M. Chiang, E. Takeuchi, M. Bradley, J. Langford and M. Winter, *Nature*, 2022, **601**, 519–525.
2 J. B. Goodenough and K. S. Park, *J. Am. Chem. Soc.*, 2013, **135**, 1167–1176.
3 C. P. Grey and D. S. Hall, *Nat. Commun.*, 2020, **11**, 6279.
4 K. Mizushima, P. C. Jones, P. J. Wiseman and J. B. Goodenough, *Mater. Res. Bull.*, 1980, **15**, 783–789.
5 T. Ohzuku and Y. Makimura, *Chem. Lett.*, 2001, 642–643.
6 T. Deng, X. Fan, L. Cao, J. Chen, S. Hou, X. Ji, L. Chen, S. Li, X. Zhou, E. Hu, D. Su, X.-Q. Yang and C. Wang, *Joule*, 2019, **3**, 2550–2564.
7 S. Liu, B. Wang, X. Zhang, S. Zhao, Z. Zhang and H. Yu, *Matter*, 2021, **4**, 1511–1527.
8 A. Manthiram, *Nat. Commun.*, 2020, **11**, 1550.
9 R. Benedek, *J. Electrochem. Soc.*, 2022, **169**, 050505.
10 H. Yu and H. Zhou, *J. Phys. Chem. Lett.*, 2013, **4**, 1268–1280.
11 M. Sathiya, G. Rousse, K. Ramesha, C. P. Laisa, H. Vezin, M. T. Sougrati, M. L. Doublet, D. Foix, D. Gonbeau, W. Walker, A. S. Prakash, M. Ben Hassine, L. Dupont and J. M. Tarascon, *Nat. Mater.*, 2013, **12**, 827–835.
12 R. A. House, J.-J. Marie, M. A. Pérez-Osorio, G. J. Rees, E. Boivin and P. G. Bruce, *Nat. Energy*, 2021, **6**, 781–789.
13 R. A. House, G. J. Rees, M. A. Pérez-Osorio, J.-J. Marie, E. Boivin, A. W. Robertson, A. Nag, M. Garcia-Fernandez, K.-J. Zhou and P. G. Bruce, *Nat. Energy*, 2020, **5**, 777–785.
14 T. Liu, J. Liu, L. Li, L. Yu, J. Diao, T. Zhou, S. Li, A. Dai, W. Zhao, S. Xu, Y. Ren, L. Wang, T. Wu, R. Qi, Y. Xiao, J. Zheng, W. Cha, R. Harder, I. Robinson, J. Wen, J. Lu, F. Pan and K. Amine, *Nature*, 2022, **606**, 305–312.
15 H. J. Yu, Y. G. So, Y. Ren, T. H. Wu, G. C. Guo, R. J. Xiao, J. Lu, H. Li, Y. B. Yang, H. S. Zhou, R. Z. Wang, K. Amine and Y. Ikuhara, *J. Am. Chem. Soc.*, 2018, **140**, 15279–15289.
16 D. Eum, B. Kim, S. J. Kim, H. Park, J. Wu, S. P. Cho, G. Yoon, M. H. Lee, S. K. Jung, W. Yang, W. M. Seong, K. Ku, O. Tamwattana, S. K. Park, I. Hwang and K. Kang, *Nat. Mater.*, 2020, **19**, 419–427.
17 J. Song, B. Li, Y. Chen, Y. Zuo, F. Ning, H. Shang, G. Feng, N. Liu, C. Shen, X. Ai and D. Xia, *Adv. Mater.*, 2020, **32**, e2000190.
18 Y. Zuo, B. Li, N. Jiang, W. Chu, H. Zhang, R. Zou and D. Xia, *Adv. Mater.*, 2018, **30**, e1707255.
19 X. Cao, H. Li, Y. Qiao, M. Jia, P. He, J. Cabana and H. Zhou, *Energy Storage Mater.*, 2021, **38**, 1–8.
20 S. Liu and H. Yu, *Sci. Bull.*, 2021, **66**, 1260–1262.
21 J. Hwang, S. Myeong, E. Lee, H. Jang, M. Yoon, H. Cha, J. Sung, M. G. Kim, D. H. Seo and J. Cho, *Adv. Mater.*, 2021, 2100352, DOI: **10.1002/adma.202100352**.
22 R. A. House, U. Maitra, M. A. Perez-Osorio, J. G. Lozano, L. Jin, J. W. Somerville, L. C. Duda, A. Nag, A. Walters, K. J. Zhou, M. R. Roberts and P. G. Bruce, *Nature*, 2020, **577**, 502–508.
23 T. Wu, X. Liu, X. Zhang, Y. Lu, B. Wang, Q. Deng, Y. Yang, E. Wang, Z. Lyu, Y. Li, Y. Wang, Y. Lyu, C. He, Y. Ren, G. Xu, X. Sun, K. Amine and H. Yu, *Adv. Mater.*, 2020, **33**, e2001358.
24 J. Hwang, S. Myeong, W. Jin, H. Jang, G. Nam, M. Yoon, S. H. Kim, S. H. Joo, S. K. Kwak, M. G. Kim and J. Cho, *Adv. Mater.*, 2020, **32**, e2001944.
25 Y. Yang, Z. Zhang, S. Liu, B. Wang, J. Liu, Y. Ren, X. Zhang, S. Zhao, D. Liu and H. Yu, *Matter*, 2022, **5**, 3869–3882.
26 L. Wang, S. Zhao, B. Wang and H. Yu, *J. Energy Chem.*, 2023, **81**, 110–117.
27 S. Ramakrishnan, B. Park, J. Wu, W. Yang and B. D. McCloskey, *J. Am. Chem. Soc.*, 2020, **142**, 8522–8531.
28 P. Liu, H. Zhang, W. He, T. Xiong, Y. Cheng, Q. Xie, Y. Ma, H. Zheng, L. Wang, Z. Z. Zhu, Y. Peng, L. Mai and D. L. Peng, *J. Am. Chem. Soc.*, 2019, **141**, 10876–10882.
29 E. Wang, Y. Zhao, D. Xiao, X. Zhang, T. Wu, B. Wang, M. Zubair, Y. Li, X. Sun and H. Yu, *Adv. Mater.*, 2020, **32**, e1906070.
30 S. Liu, J. Wan, B. Wang, C. Li, Y. Wang, L. Wang, H. Wu, N. Zhang, X. Zhang and H. Yu, *Small*, 2024, **20**, 2401497.
31 S. Liu, D. Xiao, B. Wang, L. Wang, T. Wu, Y. Wang, N. Zhang and H. Yu, *Adv. Energy Mater.*, 2023, **13**, 2300217.
32 H. Ma, H. Su, K. Amine, X. Y. Liu, S. Jaffer, T. T. Shang, L. Gu and H. J. Yu, *Nano Energy*, 2018, **43**, 1–10.
33 Y. Shi, Z. Zhang, P. Jiang, A. Gao, K. Li, Q. Zhang, Y. Sun, X. Lu, D. Cao and X. Lu, *Energy Storage Mater.*, 2021, **37**, 354–362.
34 T. Risthaus, L. Chen, J. Wang, J. Li, D. Zhou, L. Zhang, D. Ning, X. Cao, X. Zhang, G. Schumacher, M. Winter, E. Paillard and J. Li, *Chem. Mater.*, 2019, **31**, 5376–5383.
35 Y. Yang, H. Su, T. Wu, Y. Jiang, D. Liu, P. Yan, H. Tian and H. Yu, *Sci. Bull.*, 2019, **64**, 553–561.
36 J.-H. Kim, S. T. Myung, C. S. Yoon, S. G. Kang and Y. K. Sun, *Chem. Mater.*, 2004, **16**, 906–914.
37 H. Yu, Y. G. So, A. Kuwabara, E. Tochigi, N. Shibata, T. Kudo, H. Zhou and Y. Ikuhara, *Nano Lett.*, 2016, **16**, 2907–2915.
38 B. Wang, Z. Zhuo, H. Li, S. Liu, S. Zhao, X. Zhang, J. Liu, D. Xiao, W. Yang and H. Yu, *Adv. Mater.*, 2023, e2207904, DOI: **10.1002/adma.202207904**.
39 X. Li, X. Li, L. Monluc, B. Chen, M. Tang, P. H. Chien, X. Feng, I. Hung, Z. Gan, A. Urban and Y. Y. Hu, *Adv. Energy Mater.*, 2022, 2200427, DOI: **10.1002/aenm.202200427**.

40 K. Nakayama, R. Ishikawa, S. Kobayashi, N. Shibata and Y. Ikuhara, *Nat. Commun.*, 2020, **11**, 4452.
41 C. Cui, X. Fan, X. Zhou, J. Chen, Q. Wang, L. Ma, C. Yang, E. Hu, X. Q. Yang and C. Wang, *J. Am. Chem. Soc.*, 2020, **142**, 8918–8927.
42 X. Zhang, J. Zhao, G. H. Lee, Y. Liang, B. Wang, S. Liu, E. Wang, W. Yang and H. Yu, *Adv. Energy Mater.*, 2022, 2202929, DOI: **10.1002/aenm.202202929**.
43 D. Eum, S.-O. Park, H.-Y. Jang, Y. Jeon, J.-H. Song, S. Han, K. Kim and K. Kang, *Nat. Mater.*, 2024, **23**, 1093–1099.
44 X. Cao, H. Li, Y. Qiao, P. He, Y. Qian, X. Yue, M. Jia, J. Cabana and H. Zhou, *Joule*, 2022, **6**, 1290–1303.
45 N. Li, M. Sun, W. H. Kan, Z. Zhuo, S. Hwang, S. E. Renfrew, M. Avdeev, A. Huq, B. D. McCloskey, D. Su, W. Yang and W. Tong, *Nat. Commun.*, 2021, **12**, 2348.
46 J. Kim and A. Manthiram, *Nature*, 1997, **390**, 265–267.
47 C. Julien, *Solid State Ionics*, 2000, **136–137**, 887–896.
48 C. Julien, *Solid State Ionics*, 2006, **177**, 11–19.
49 Y. Pei, S. Li, Q. Chen, R. Liang, M. Li, R. Gao, D. Ren, Y.-P. Deng, H. Jin, S. Wang, D. Su, Y. Hu and Z. Chen, *J. Mater. Chem. A*, 2021, **9**, 2325–2333.
50 Z. Zhuo, K. Dai, R. Qiao, R. Wang, J. Wu, Y. Liu, J. Peng, L. Chen, Y.-d. Chuang, F. Pan, Z.-x. Shen, G. Liu, H. Li, T. P. Devereaux and W. Yang, *Joule*, 2021, **5**, 975–997.
51 T. Wu, X. Zhang, Y. Wang, N. Zhang, H. Li, Y. Guan, D. Xiao, S. Liu and H. Yu, *Adv. Funct. Mater.*, 2022, **33**, 2210154.
52 K. Luo, M. R. Roberts, R. Hao, N. Guerrini, D. M. Pickup, Y. S. Liu, K. Edstrom, J. Guo, A. V. Chadwick, L. C. Duda and P. G. Bruce, *Nat. Chem.*, 2016, **8**, 684–691.
53 J. Rana, J. K. Papp, Z. Lebens-Higgins, M. Zuba, L. A. Kaufman, A. Goel, R. Schmuch, M. Winter, M. S. Whittingham, W. Yang, B. D. McCloskey and L. F. J. Piper, *ACS Energy Lett.*, 2020, **5**, 634–641.
54 Q. Li, D. Ning, D. Zhou, K. An, G. Schuck, D. Wong, W. Kong, C. Schulz, G. Schumacher and X. Liu, *Chem. Mater.*, 2020, **32**, 9404–9414.
55 X. Ding, D. Luo, J. Cui, H. Xie, Q. Ren and Z. Lin, *Angew. Chem., Int. Ed.*, 2020, **59**, 7778–7782.
56 Y. Wang, L. Wang, X. Guo, T. Wu, Y. Yang, B. Wang, E. Wang and H. Yu, *ACS Appl. Mater. Interfaces*, 2020, **12**, 8306–8315.